Amorphous Phase-Mediated Crystallization of Ni Nanocrystals
Revealed by High-Resolution Liquid Phase Electron Microscopy

Jiwoong Yang,[†,‡,§,‖] Jahyun Koo,[⊥] Seulwoo Kim,[‡] Sungho Jeon,[#] Back Kyu Choi,[†,‡] Sangwoo Kwon,[‡] Joodeok Kim,[†,‡] Byung Hyo Kim,[†,‡] Won Chul Lee,[#] Won Bo Lee,[‡] Hoonkyung Lee,[⊥] Taeghwan Hyeon,[†,‡,*] Peter Ercius,[‖,*] and Jungwon Park[†,‡,*]

[†]Center for Nanoparticle Research, Institute for Basic Science (IBS), Seoul 08826, Republic of Korea

[‡]School of Chemical and Biological Engineering, Institute of Chemical Processes, Seoul National University, Seoul 08826, Republic of Korea

[§]Materials Sciences Division and [‖]Molecular Foundry, Lawrence Berkeley National Laboratory, Berkeley, California 94720, United States

[⊥]Department of Physics, Konkuk University, Seoul 05029, Republic of Korea

[#]Department of Mechanical Engineering, Hanyang University, Ansan, Gyeonggido, 15588, Republic of Korea

Supporting Information Placeholder

ABSTRACT: Nonclassical features of crystallization in solution have been recently identified both experimentally and theoretically. Especially, amorphous phase-mediated pathway is found in various systems of crystallization as an important route, different from classical nucleation and growth model. Here, we utilize high-resolution *in-situ* transmission electron microscopy with graphene liquid cells to study amorphous phase-mediated formation of Ni nanocrystals. An amorphous phase is precipitated in the initial stage of the reaction. Within the amorphous particles, crystalline domains nucleate and eventually form nanocrystals. In addition, unique crystallization behaviors, such as formation of multiple domains and dislocation relaxation, are observed in amorphous phase-mediated crystallization. Theoretical calculations confirm that surface interactions can induce amorphous precipitation of metal precursors, which is analogous to the surface-induced amorphous-to-crystalline transformation occurring in biomineralization. Our results imply that an unexplored nonclassical growth mechanism is important for the formation of nanocrystals.

Crystallization in liquid media is ubiquitous phenomena and is fundamental to understanding the formation of many materials including colloids, biominerals, and nanocrystals.[1] In the classical theory of colloidal chemistry, crystallization is described by nucleation and growth where it is assumed that lattices are formed by ion-by-ion addition.[1,2] Recently, nonclassical features of crystallization have been identified.[3-5] In particular, amorphous phases formed at the initial stage of crystallization are known to provide an important free-energy landscape for materials formation.[3,5c-e,6] Amorphous phase-mediated crystallization processes have been mainly observed in biomineralization processes such as the formation of protein[3d,e] and calcium phosphate/calcite.[5c,5d,6] However, many questions regarding its interplay with classical pathways and generality in different materials are less explored and await experimental approaches. A major difficulty for the study of this phenomenon originates from the lack of characterization methods for direct observation of the process with a high spatial and temporal resolution. The recent development of liquid phase *in-situ* transmission electron microscopy (TEM) provides the new capabilities for the direct and real-time observation of material dynamics in liquid media,[5,7,8] which have not been accessible by the other characterization tools.[9] Combining it with the technical advances in TEM, such as aberration-corrector optics,[10] enables the *in-situ* image acquisition with high-resolution (HR). Thus, resolving different phases and crystallinity of materials in liquid becomes possible.

Here, we present the direct HR observation of amorphous phase-mediated Ni nanocrystal (NC) formation by graphene liquid cell (GLC) TEM. We encapsulated a molecular precursor solution for Ni NC formation in GLCs for *in-situ* TEM observation. Atomic resolution TEM imaging shows distinct stages of Ni NC formation. An amorphous phase is rapidly aggregated from the homogenous solution. Then, the nucleation and growth of crystalline domains drive the formation of Ni NCs. The experimental result is supported by theoretical calculations. Interestingly, this process is similar to the surface mediated amorphous-to-crystalline transition of biominerals in reduction reaction-limited manners. In addition, multiple nucleation of crystalline phase in a single amorphous aggregate and relaxation of

dislocations at grain boundaries are also observed, which highlights the diversity in the NC formation pathways.

We imaged Ni NC formation in GLCs[11] using a TEM with chromatic and spherical aberration correction (Figure S1 and Supporting Information 1.1–1.3 for experimental details). A homogeneous Ni (II) growth solution containing Ni-ammine-acetate complexes (Figure S2) was prepared and encapsulated in GLCs. Using GLCs minimizes undesired scattering of the electron beam.[11,12] As a result, the direct observation in GLCs secures a sufficiently high contrast and spatial resolution for observing the first-row transition metal in solution, otherwise obscured by background noise. Low-resolution
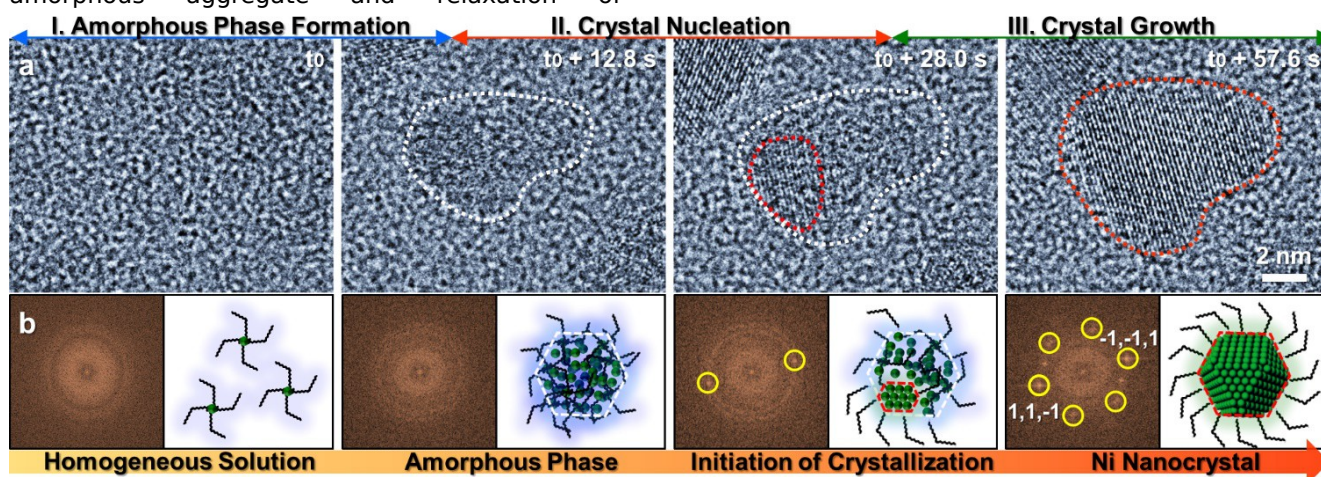

Figure 1. Overall view on amorphous phase-mediated formation of Ni NCs. (a) Representative TEM images showing the reaction stages of amorphous phase-mediated crystallization: (i) Amorphous phase formation, (ii) crystal nucleation, and (iii) crystal growth. The white and red dashed lines represent the amorphous and crystalline phases, respectively. (b) The corresponding FFT images and schematic illustrations.

in-situ TEM movies (Figure S3 and Movie S1) present the overview of the Ni NC formation. The formation of Ni NCs is confirmed by TEM images, electron energy loss spectroscopy and energy dispersive X-ray spectroscopy (Figure S4). Nanoparticles (NPs) are recognized by the evolution of dots with dark contrast and they grow into sub-ten nanometers.

HR *in-situ* TEM observation shows a temporal view of individual NC formation (Figure 1, Movie S2). At the early stage, an amorphous phase precipitates from the homogeneous solution. Within the domain marked with white dashed lines (Figure 1a), aggregated intermediates show randomly packed granular features (Movie S2 and S3). TEM simulations support that the domain does not contain crystalline species (Figures S5 and S6).[13] A crystalline domain (mapped by red dashed lines) nucleates from the corner as it is

clearly identified by the lattice fringe formation (Figure 1a). Then, crystalline domains grow gradually whereas the remainder of the NP maintains an amorphous phase with the slight increase of overall NP size. Eventually, the entire domain transforms into the face-centered cubic (fcc) crystalline phase of Ni,[14] which is clearly identified from bright field images and the fast Fourier-transform (FFT) patterns (Figure 1b). Such growth pattern is different from the classical growth mechanism of colloidal NCs under the diffusion limited growth condition. Conventionally, NCs nucleate stochastically at the initial stage, followed by the increase of their size throughout the growth due to the gradual monomer attachments and/or coalescence events.[2,15] Additional HR *in-situ* (Figure S7 and Movie S3) and wide-view movies (Movie S4) present the similar formation pathway, suggesting that the amorphous phase-mediated crystalli-
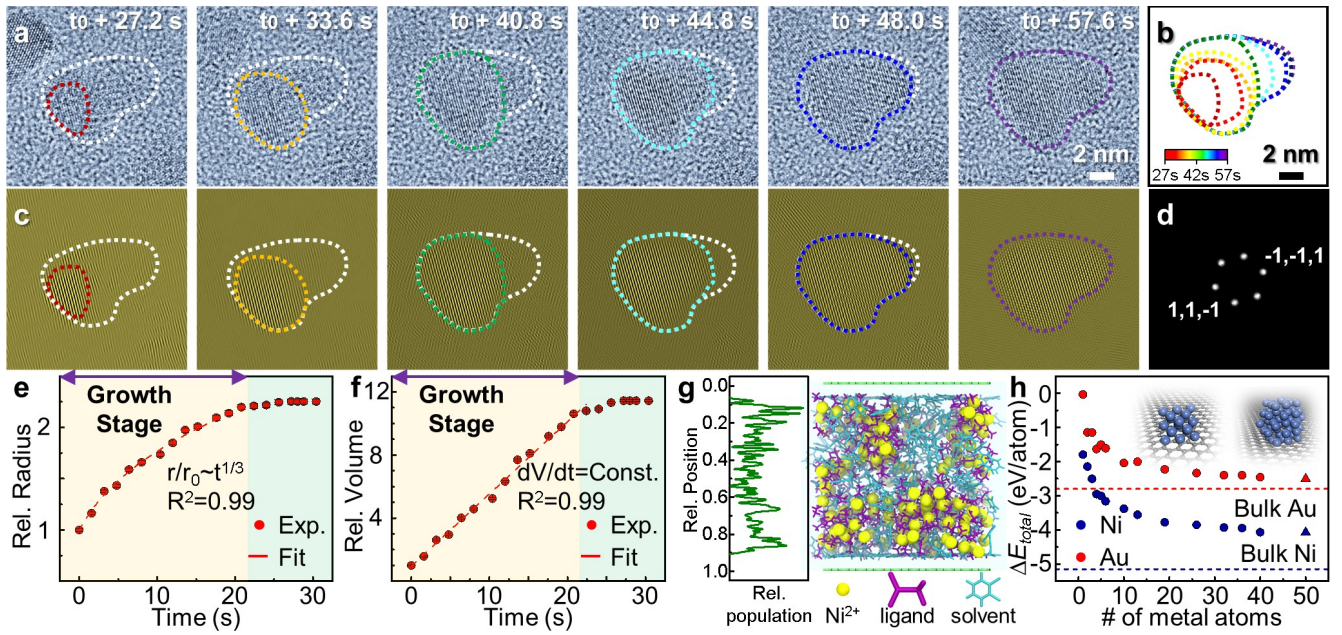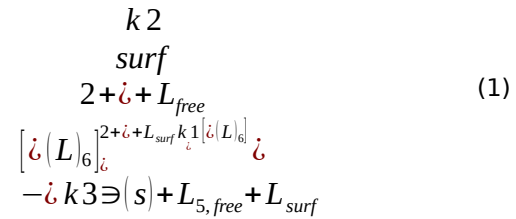
Figure 2. Crystalline phase formation. (a) A time-series of TEM images showing the growth of the crystalline phase from the amorphous phase, (b) the corresponding contour plot, and (c) inverse FFT images. The corresponding movie is displayed in Movie S2. (d) FFT of the last image frame. (e,f) Growth kinetics of the crystalline domain shown in time-dependent change of the relative radius (e) and volume (f). The first frame at t_0+ 27.2 s is set as the standard for plotting. (g) MD calculations showing the distribution of Ni^{2+} ions in GLC. (h) DFT calculation estimating the formation energy of Ni (blue) and Au (red) NPs as a function of the number of metal atoms, where dots and triangles denote the crystalline and amorphous NPs, respectively. The blue and red dashed lines represent the formation energy of bulk Ni and Au crystals. The inset images show the structure models for Ni_{19} and Ni_{50}.

zation of Ni NCs occurs ubiquitously. Seeing the burst of NC formation in a low magnification movie, it is likely that the formation of amorphous phases occurs relatively quickly at the earlier stage and the on-set of amorphous to crystalline transformation takes place stochastically over a prolonged time period.

To gain a better understanding of the process, we analyze the growth of the crystalline domains in more detail. To locate crystalline domains at different time frames (Figure 2a,b), we perform masking and inverse FFT of bright field TEM images (Figure 2c,d). This enables us to trace the growth kinetics of the crystalline domains (Figure 2e,f). The analysis results of another Ni NC from Movie S3 are shown in Figures S8 and S9, showing the consistent results. It has been known that one of the major reaction pathways for the amorphous-to-crystalline transformation in biomineralization is induced by surface interactions.[6] It is likely that the amorphous phase observed in our experiments is an amorphous intermediate precipitated on the graphene surface. This is supported by the fact that the translational and rotational motion of NCs are significantly suppressed during their growth (Figure 2c,d). It is also well known that bulk Ni metal strongly interacts with graphene.[16] These facts suggest a hypothesis that the process we observed is comparable to the surface induced amorphous-to-crystalline transformation. Interestingly, the detailed reaction mechanism can be adopted from the Ni electroplating process,[17]

$$[\i(L)_6]^{2+\i} \xrightarrow{k2}_{surf} 2+\i+L_{free} \tag{1}$$

$$[\i(L)_6]_{\i} \xrightarrow{k1[\i(L)_6]}_{\i} \i -\i k3 \ni (s)+L_{5,free}+L_{surf} \tag{2}$$

$$[\i(L)_6]^{\i}_{surf} \to 2+\i+2e^{\i}$$

where, L is an organic ligand molecule. The precipitation of aggregates on the graphene surface and the subsequent crystallization is analogous to reactions (1) and (2), respectively. The reduction reaction is presumably the rate-determining reaction of the crystal generation because the amorphous intermediates are rapidly formed at the initial stage. Thus, *dV/dt* is approximately proportional to
$$k_3 \i \frac{\i \i \i e^{\i}}{-\i} \frac{\i}{[\i(L)_6]^{\i}_{surf}} 2+\i$$
, which is almost constant since the concentration of Ni complexes in aggregates and the electron dose rate are unchanged. The crystal growth rate (*dV/dt*) is measured as a constant for each NC and the growth is completed earlier at the higher dose

rate (Figure 2e,f and Figure S9), which is consistent with our suggestion.

Furthermore, the suggested formation mechanism is supported by theoretical calculations. Molecular dynamic (MD) calculations show that Ni^{2+} ions tend to form aggregates on the graphene surface (Figure 2g and Figure S10). We also estimate the formation energy of NPs on graphene as a function of the number of atoms by density functional theory (DFT) (Figure 2h). The atomic structures of the NPs used for calculations are displayed in Figure S11. The formation energy of Ni NPs decreases as the size of the NPs increases. Surprisingly, the amorphous Ni NPs on graphene (50 atoms in Figure 2h) show similar formation energy as crystalline ones, indicating that substrate interaction contributes to stabilizing amorphous phases. In addition, the surface energy of an amorphous NP is lower than that of a crystalline NP, which helps to expedite the formation of amorphous intermediates (Table S1). It is noteworthy that the formation energy of Ni NPs on graphene is much lower than that of Au NPs. Previous reports show that noble metal NCs typically grow by the classical nucleation and growth model.[11] This implies that interactions with a substrate can guide an alternative growth pathway such as the rapid amorphous condensation and subsequent crystallization process seen in the reported experiments.

As nucleation of crystalline domain is stochastic, such events may occur at multiple sites within a single amorphous aggregate. Our HR in-situ TEM imaging shows the sequential nucleation of multiple crystalline grains in the one amorphous aggregate (Figure 3a and Movie S5). The corresponding Fourier filtered images mapping these domains are displayed in Figure S12. In the initial stage, the first crystalline domain, marked with the red dashed line, is formed at the local region of the amorphous aggregate and expands. Then, another crystalline domain appears in a different region, which is indicated by the yellow dashed lines (Figure 3a). The nucleation and propagation of the last crystalline domain marked with the blue color follows in the later stage (Figure 3a). Consequently, the resulting Ni NC in the last image at $t_0+201.6$ s, shows the coexistence of three crystalline domains with the sharp interfaces. We readily find populations of both single and polycrystalline NCs from the same experiment (Figure S13), highlighting diversity in the crystallization pathways. Coalescence of small NCs along the specific crystal direction that minimizes the entropic barrier provided by surface capping ligands has been suggested as one of the major growth mechanisms of colloidal metal NCs with multiple domains.[5a,11a,b] Our direct observation implies that the formation of multiple crystalline grains in the amorphous phase-mediated crystallization can be an alternative pathway for the formation of multi-grained NCs.
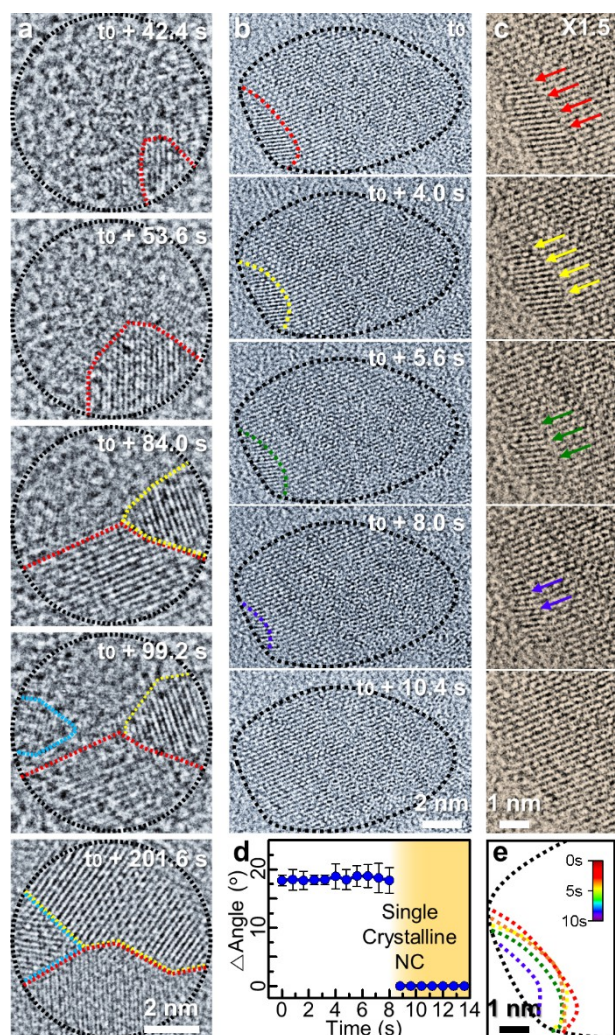
Figure 3. Multiple nucleation and dislocation relaxation. (a) A time-series TEM images showing multiple nucleation. The color lines highlight three crystalline domains. The corresponding movie is displayed in Movie S5. (b) A time-series TEM images of dislocation relaxation. The dashed lines highlight the grain boundary. The corresponding movie is displayed in Movie S6. (c) Magnified TEM images around the boundary without the dashed lines. (d) The relative misorientations between two crystal domains in the panel (b). (e) The contour plot showing the dislocation relaxation.

Furthermore, we observe the relaxation of a dislocation in a polycrystalline NC to form a single-crystalline NC (Figure 3b–e and Movie S6). The dislocation in Figure 3b,c is formed by two crystalline domains with a large difference in their sizes. The boundary is intrinsically curved and kinked. Such a dislocation is presumably thermodynamically unstable. During the relaxation, the kink, in the first image of Figure 3b,c at t_0, is first removed by the fast incursion of the dominant domain into the region near the kink, thus, the boundary develops a smooth curvature. The grain boundary is, then, gradually expelled until it completely leaves the NC (Figure 3e). The two domains keep a sharp interface and the relative crystal orientation during the movement of the grain boundary (Figure 3d). The

NC also maintains its overall size and shape. Considering that grain boundaries in other polycrystalline NCs (Figure 3a, Movie S6 and Figure S13) are well preserved even at the higher dose rate, the relaxation process may be mainly induced by the small misorientation and the large size disparity between adjunct crystal domains.[11b]

In summary, we report the direct observation of amorphous phase-mediated crystallization of Ni NCs using GLC TEM. Our results uncover an unexplored reaction pathway of NC synthesis and highlight the diversity in crystallization processes.

ASSOCIATED CONTENT

Supporting Information

The Supporting Information is available free of charge on ACS Publications website at DOI:
Methods; additional TEM and spectroscopy data (PDF)
Movie S1–S6: *In-situ* TEM movies (avi)

AUTHOR INFORMATION

Corresponding Author

*E-mail: jungwonpark@snu.ac.kr (J.P.); percius@lbl.gov (P.E.); thyeon@snu.ac.kr (T.H.)

Notes

The authors declare no competing financial interests.

REFERENCES

(1) (a) Sugimoto, T. Preparation of monodispersed colloidal particles. *Adv. Colloid Interfac. Sci.* **1987**, *28*, 65–108. (b) De Yoreo, J.; Vekilov, P. G. Principles of crystal nucleation and growth. *Rev. Miner. Geochem.* **2003**, *54*, 57−93. (c) Sohn, S.; Xie, Y.; Jung, Y.; Schroers, J.; Cha, J. J. Tailoring crystallization phases in metallic glass nanorods via nucleus starvation. *Nat. Commun.* **2017**, 8, 1980.

(2) (a) Talapin, D. V.; Rogach, A. L.; Haase, M.; Weller, H. Evolution of an ensemble of nanoparticles in a colloidal solution: Theoretical study. *J. Phys. Chem. B* **2001**, *105*, 12278–12285. (b) Bullen, C. R.; Mulvaney, P. Nucleation and growth kinetics of CdSe nanocrystals in octadecene. *Nano Lett.* **2004**, *4*, 2303–2307. (c) Owen, J. S.; Chan, E. M.; Liu, H.; Alivisatos, A. P. Precursor conversion kinetics and the nucleation of cadmium selenide nanocrystals. *J. Am. Chem. Soc.* **2010**, *132*, 18206−18213. (d) Baumgartner, J.; Dey, A.; Bomans, P. H. H.; Coadou, C. L.; Fratzl, P.; Sommerdijk, N. A. J. M.; Faivre, D. Nucleation and growth of magnetite from solution. *Nat. Mater.* **2013**, *12*, 310−314.

(3) (a) Gebauer, D.; Kellermeier, M.; Gale, J. D.; Bergströmc, L.; Cölfen, H. Pre-nucleation clusters as solute precursors in crystallisation. *Chem. Soc. Rev.* **2014**, *43*, 2348–2371. (b) De Yoreo, J. J.; Gilbert, P. U. P. A.; Sommerdijk, N. A. J. M.; Penn, R. L.; Whitelam, S.; Joester, D.; Zhang, H.; Rimer, J. D.; Navrotsky, A.; Banfield, J. F.; Wallace, A. F.; Michel, F. M.; Meldrum, F. C.; Cölfen, H.; Dove, P. M. Crystallization by particle attachment in synthetic, biogenic, and geologic environments. *Science* **2015**, *349*, aaa6760. (c) Lee, J.; Yang, J.; Kwon, S. G.; Hyeon, T. Nonclassical nucleation and growth of inorganic nanoparticles. *Nat. Rev. Mater.* **2016**, *1*, 16034. (d) Yamazaki, T.; Kimura, Y.; Vekilov, P. G.; Furukawa, E.; Shirai, M.; Matsumoto, H.; Van Driessche, A. E. S.; Tsukamoto K. Two types of amorphous protein particles facilitate crystal nucleation. *Proc. Natl. Acad. Sci. U.S.A.* 2017, *114*, 2154–2159. (e) Sleutel, M.; Van Driessche, A. E. S. Nucleation of protein crystals–a nanoscopic perspective *Nanoscale* **2018**, *10*, 12256–12267.

(4) (a) Schliehe, C.; Juarez, B. H.; Pelletier, M.; Jander, S.; Greshnykh, D.; Nagel, M.; Meyer, A.; Foerster, S.; Kornowski, A.; Klinke, C.; Weller, H. Ultrathin PbS sheets by two-dimensional oriented attachment. *Science* **2010**, *329*, 550–553. (b) Liu, Y.-H.; Wang, F.; Wang, Y.; Gibbons, P. C.; Buhro, W. E. Lamellar assembly of cadmium selenide nanoclusters into quantum belts. *J. Am. Chem. Soc.* **2011**, *133*, 17005–17013. (c) Langille, M. R.; Zhang, J.; Personick, M. L.; Li, S.; Mirkin, C. A. Stepwise evolution of spherical seeds into 20-fold twinned icosahedra. *Science* **2012**, *337*, 954–957. (d) Yang, J.; Muckel, F.; Baek, W.; Fainblat, R.; Chang, H.; Bacher, G.; Hyeon, T. Chemical synthesis, doping, and transformation of magic-sized semiconductor alloy nanoclusters. *J. Am. Chem. Soc.* **2017**, *139*, 6761–6770.

(5) (a) Zheng, H.; Smith, R. K.; Jun, Y.-w.; Kisielowski, C.; Dahmen, U.; Alivisatos, A. P. Observation of single colloidal platinum nanocrystal growth trajectories. *Science* **2009**, *324*, 1309–1312. (b) Zhu, C.; Liang, S.; Song, E.; Zhou, Y.; Wang, W.; Shan, F.; Shi, Y.; Hao, C.; Yin, K.; Zhang, T.; Liu, J.; Zheng, H.; Sun, L. In-situ liquid cell transmission electron microscopy investigation on oriented attachment of gold nanoparticles. *Nat. Commun.* **2018**, *9*, 421. (c) Nielsen, M. H.; Aloni, S.; De Yoreo, J. J. In situ TEM imaging of CaCO3 nucleation reveals coexistence of direct and indirect pathways. *Science* **2014**, *345*, 1158–1162. (d) Smeet, P. J. M.; Cho, K. R.; Kempen, R. G. E.; Sommerdijk, N. A. J. M.; De Yoreo, J. J. Calcium carbonate nucleation driven by ion binding in a biomimetic matrix revealed by in situ electron microscopy. *Nat. Mater.* **2015**, *14*, 394–399. (e) Loh, N. D.; Sen, S.; Bosman, M.; Tan, S. F.; Zhong, J.; Nijhuis, C. A.; Král, P.; Matsudaira, P.; Mirsaidov, U. Multistep nucleation of nanocrystals in aqueous solution. *Nat. Chem.* **2017**, *9*, 77–82.

(6) (a) Xu, G.; Yao, N.; Aksay, I. A.; Groves, J. T. Biomimetic synthesis of macroscopic-scale calcium carbonate thin films. Evidence for a multistep assembly process. *J. Am. Chem. Soc.* **1998**, *120*, 11977–11985. (b) Addadi, L.; Raz, S.; Weiner, S. Taking advantage of disorder: Amorphous calcium carbonate and its roles in biomineralization *Adv. Mater.* **2003**, *15*, 959–970. (c) Politi, Y.; Arad, T.; Klein, E.; Weiner, S.; Addadi, L. Sea urchin spine calcite forms via a transient amorphous calcium carbonate phase. *Science* **2004**, *306*, 1161–1164. (d) Gebauer, D.; Volkel, A.; Cölfen, H. Stable prenucleation calcium carbonate clusters. *Science* **2008**, *322*, 1819–1822. (e) Dey, A.; Bomans, P. H. H.; Muller, F. A.; Will, J.; Frederik, P. M.; de With, G.; Sommerdijk, N. A. J. M. The role of prenucleation clusters in surface-induced calcium phosphate crystallization. *Nat. Mater.* **2010**, *9*, 1010–1014. (f) Jin, W.; Jiang, S.; Pan, H.; Tang, R. Amorphous phase mediated crystallization: Fundamentals of biomineralization. *Crystals* **2018**, *8*, 48.

(7) (a) de Jonge, N.; Ross, F. M. Electron microscopy of specimens in liquid. *Nat. Nanotechnol.* **2011**, *6*, 695–704. (b) Ross, F. M. Opportunities and challenges in liquid cell electron microscopy. *Science* **2015**, *350*, aaa9886. (c) De Yoreo, J. J.; Sommerdijk N. A. J. M. Investigating materials formation with liquid-phase and cryogenic TEM. *Nat. Rev. Mater.* **2016**, *1*, 16035. (d) Lou, B.; Smith, J. W.; Ou, Z.; Chen, Q. Quantifying the self-assembly behavior of anisotropic nanoparticles using liquid-phase transmission electron microscopy. *Acc. Chem. Res.* **2017**, *50*, 1125–1133. (e) Zeng, Z.; Zheng, W.; Zheng, H. Visualization of colloidal nanocrystal formation and electrode–electrolyte interfaces in liquids using TEM. *Acc. Chem. Res.* **2017**, *50*, 1808–1817. (f) Tan, S. F.; Chee, S. W.; Lin, G.; Mirsaidov, U. Direct Observation of interactions between nanoparticles and nanoparticle self-assembly in solution. *Acc. Chem. Res.* **2017**, *50*, 1303–1312. (g) Kim, B. H.; Yang, J.; Lee, D.; Choi, B. K.; Hyeon, T.; Park, J. Liquid-phase transmission electron microscopy for studying colloidal inorganic nanoparticles. *Adv. Mater.* **2018**, *30*, 1703316.

(8) (a) Williamson, M. J.; Tromp, R. M.; Vereecken, P. M.; Hull, R.; Ross, F. M. Dynamic microscopy of nanoscale cluster growth at the solid-liquid interface. *Nat. Mater.* **2003**, *2*, 532–536. (b) Liao, H.-G.; Cui, L.; Whitelam, S.; Zheng, H. Real-time imaging of Pt₃Fe nanorod growth in solution. *Science* **2012**, *336*, 1011–1014. (c) Patterson, J. P.; Abellan, P.; Denny, M. S. Jr.; Park, C.; Browning, N. D.; Cohen, S. M.; Evans, J. E.; Gianneschi, N. C. Observing the growth of metal-organic frameworks by in situ liquid cell transmission electron microscopy. *J. Am. Chem. Soc.* **2015**, *137*, 7322–7328. (d) Kim, J.; Jones, M. R.; Ou, Z.; Chen, Q. In situ electron microscopy imaging and quantitative structural modulation of nanoparticle superlattices. *ACS Nano* **2016**, *10*, 9801–9808. (e) Sutter, E.; Sutter, P.; Tkachenko, A. V.; Krahne, R.; de Graaf, J.; Arciniegas M.; Manna, L. In situ microscopy of the self-assembly of branched nanocrystals in solution. *Nat. Commun.* **2016**, *7*, 11213.

(9) (a) Qu, L.; Yu, W. W.; Peng, X. In situ observation of the nucleation and growth of CdSe nanocrystals. *Nano Lett.* **2004**, *4*, 465–469. (b) Kudera, S.; Zanella, M.; Giannini, C.; Rizzo, A.; Li, Y.; Gigli, G.; Cingolani, R.; Ciccarella, G.; Spahl, W.; Parak, W. J.; Manna, L. Sequential growth of magic-size CdSe nanocrystals. *Adv. Mater.* **2007**, *19*, 548–552. (c) Liu, H.; Owen, J. S.; Alivisatos, A. P. Mechanistic study of precursor evolution in colloidal group II-VI semiconductor nanocrystal synthesis. *J. Am. Chem. Soc.* **2007**, *129*, 305–312. (d) Kwon, S. G.; Krylova, G.; Phillips, P. J.; Klie, R. F.; Chattopadhyay, S.; Shibata, T.; Bunel, E. E.; Liu, Y.; Prakapenka, V. B.; Lee, B.; Shevchenko, E. V. Heterogeneous nucleation and shape transformation of multicomponent metallic nanostructures. *Nat. Mater.* **2015**, *14*, 215–223. (e) Xie, L.; Shen, Y.; Franke, D.; Sebastián, V.; Bawendi, M. G.; Jensen, K. F. Characterization of indium phosphide quantum dot growth intermediates using MALDI-TOF mass spectrometry. *J. Am. Chem. Soc.* **2016**, *138*, 13469–13472. (f) Yu, K.; Liu, X.; Qi, T.; Yang H.; Whitfield D. M.; Chen Q. Y.; Huisman, E. J., Hu, C. General low-temperature reaction pathway from precursors to monomers before nucleation of compound semiconductor nanocrystals. *Nat. Commun.* **2016**, *7*, 12223. (g) Kim, S.; Jung, H. J.; Kim, J. C.; Lee, K.-S.; Park, S. S.; Dravid, V. P.; He, K.; Jeong, H. Y. In situ observation of resistive switching in an asymmetric graphene oxide bilayer structure. *ACS Nano* **2018**, *12*, 7335–7342. (h) Yang, J.; Muckel, F.; Choi, B. K.; Lorenz, S.; Kim, I. Y.; Ackermann, J.; Chang, H.; Czerney, T.; Kale, V. S.; Hwang, S.-J.; Bacher, G.; Hyeon, T. Co²⁺-doping of magic-sized CdSe clusters: Structural insights via ligand field transitions. *Nano Lett.* **2018**, *18*, 7350–7357.

(10) (a) Rossell, M.; Watanabe, M.; Erni, R.; Radmilovic, V.; Dahmen, U. Quantitative Li mapping in Al alloys by sub-eV resolution energy-filtering transmission electron microscopy (EFTEM) in the aberration-corrected, monochromated TEAM0.5 instrument. *Microsc. Microanal.* **2009**, *15*, 430–431. (b) Pennycook, S. J. The impact of STEM aberration correction on materials science. *Ultramicroscopy* **2017**, *180*, 22–23.

(11) (a) Yuk, J. M.; Park, J.; Ercius, P.; Kim, K.; Hellebusch, D. J.; Crommie, M. F.; Lee, J. Y.; Zettl, A.; Alivisatos, A. P. High-resolution EM of colloidal nanocrystal growth using graphene liquid cells. *Science* **2012**, *336*, 61–64. (b) Park, J.; Elmlund, H.; Ercius, P.; Yuk, J. M.; Limmer, D. T.; Chen, Q.; Kim, K.; Han, S. H.; Weitz, D. A.; Zettl, A.; Alivisatos, A. P. 3D structure of individual nanocrystals in solution by electron microscopy. *Science* **2015**, *349*, 290–295. (c) Chen, Q.; Smith, J. M.; Park, J.; Kim, K.; Ho, D.; Rasool, H. I., Zettl, A., Alivisatos, A. P. 3D motion of DNA-Au nanoconjugates in graphene liquid cell electron microscopy. *Nano Lett.* **2013**, *13*, 4556–4561. (d) Textor, M.; de Jonge, N. Strategies for preparing graphene liquid cells for transmission electron microscopy. *Nano Lett.* **2018**, *18*, 3313–3321.

(12) de Jonge, N. Theory of the spatial resolution of (scanning) transmission electron microscopy in liquid water or ice layers. *Ultramicroscopy* **2018**, *187*, 113–125.

(13) Li, L.; Wang, L.-L.; Johnson, D. D.; Zhang, Z.; Sanchez, S. I.; Kang, J. H.; Nuzzo, R. G.; Wang, Q.; Frenkel, A. I.; Li, J.; Ciston, J.; Stach, E. A.; Yang, J. C. Noncrystalline-to-crystalline transformations in Pt nanoparticles. *J. Am. Chem. Soc.* **2013**, *135*, 13062–13072.

(14) Richard-Plouet, M.; Guillot, M.; Vilminot, S.; Leuvrey, C.; Estournés, C.; Kurmoo, M. hcp and fcc nickel nanoparticles prepared from organically functionalized layered phyllosilicates of nickel(II). *Chem. Mater.* **2007**, *19*, 865–871.

(15) (a) Sutter, E. A.; Sutter, P. W. Determination of redox reaction rates and orders by in situ liquid cell electron microscopy of Pd and Au solution growth. *J. Am. Chem. Soc.* **2014**, *136*, 16865–16870. (b) Liao, H.-G.; Zherebetskyy, D.; Xin, H.; Czarnik, C.; Ercius, P.; Elmlund, H.; Pan, M.; Wang, L.-W.; Zheng, H. Facet development during platinum nanocube growth. *Science* **2014**, *345*, 916–919. (c) Liang, W.; Zhang, X.; Pan, Z. M.; Czarnik, C.; Bustillo, K.; Xu, J.; Chu, Y.; Zheng, H. In situ study of Fe_3Pt-Fe_2O_3 core-shell nanoparticle formation. *J. Am. Chem. Soc.* **2015**, *137*, 14850–14853.

(16) (a) Dahal, A.; Batzill, M. Graphene–nickel interfaces: a review. *Nanoscale*, **2014**, *6*, 2548–2562. (b) Yang, J.; Kim, K.; Lee, Y.; Kim, K.; Lee, W. C.; Park, J. Self-organized growth and self-assembly of nanostructures on 2D materials. *FlatChem* **2017**, *5*, 50–68.

(17) (a) Guglielmi, N. Kinetics of the deposition of inert particles from electrolytic baths. *J. Electrochem. Soc.* **1972**, *119*, 1009–1012. (b) Ruvinskii, O. E. Investigation of mechanism of electrorecudtion of aquo ions of nickel (2+) and iron (2+). *Soviet Electrochem.* **1975**, *11*, 109–111.

Table of Contents Graphic for

**"Amorphous Phase-Mediated Crystallization of Ni Nanocrystals
Revealed by High-Resolution Liquid Phase Electron Microscopy"**